remote sensing

MDPI

Article

An Automatic Method for Delimiting Deformation Area in InSAR Based on HNSW-DBSCAN Clustering Algorithm

Jianfeng Han [1], Xuefei Guo [1], Runcheng Jiao [1,*], Yun Nan [1], Honglei Yang [2], Xuan Ni [1], Danning Zhao [1], Shengyu Wang [1], Xiaoxue Ma [1], Chi Yan [1], Chi Ma [1] and Jia Zhao [1]

[1] Beijing Institute of Geological Hazard Prevention, Beijing 100120, China; 2012190023@cugb.edu.cn (J.H.); 1012132206@cugb.edu.cn (X.N.); 2012200025@cugb.edu.cn (D.Z.); 201521490007@mail.bnu.edu.cn (C.M.)
[2] School of Land Science and Technology, China University of Geosciences, Beijing 100083, China; hongleiyang@cugb.edu.cn
* Correspondence: 1012151216@cugb.edu.cn

Abstract: InSAR (Interferometric Synthetic Aperture Radar) is widely recognized as a crucial remote sensing tool for monitoring various geological disasters because it provides all-day and all-weather monitoring. Nevertheless, the current interpretation methods for InSAR heavily depend on the interpreter's experience, which hinders efficiency and fails to meet the requirements for the timely detection of geologic hazards. Furthermore, the results obtained through current InSAR processing carry inherent noise interference, further complicating the interpretation process. To address those issues, this paper proposes an approach that enables automatic and rapid identification of deformation zones. The proposed method leverages IPTA (Interferometric Point Target Analysis) technology for SAR data processing. It combines the power of HNSW (Hierarchical Navigable Small Word) and DBSCAN (Density-Based Spatial Clustering of Applications with Noise) algorithms to cluster deformation results. Compared with traditional methods, the computational efficiency of the proposed method is improved by 11.26 times, and spatial noise is suppressed. Additionally, the clustering results are fused with slope units determined using DEM (Digital Elevation Model), which facilitates the automatic identification of slopes experiencing deformation. The experimental verification in the western mountainous area of Beijing has identified 716 hidden danger areas, and this method is superior to the traditional technology in speed and automation.

Keywords: InSAR; IPTA; HNSW; DBSCAN; Beijing

Citation: Han, J.; Guo, X.; Jiao, R.; Nan, Y.; Yang, H.; Ni, X.; Zhao, D.; Wang, S.; Ma, X.; Yan, C.; et al. An Automatic Method for Delimiting Deformation Area in InSAR Based on HNSW-DBSCAN Clustering Algorithm. *Remote Sens.* **2023**, *15*, 4287. https://doi.org/10.3390/rs15174287

Academic Editor: Salvatore Stramondo

Received: 15 July 2023
Revised: 20 August 2023
Accepted: 28 August 2023
Published: 31 August 2023

1. Introduction

With the progress of society, more and more attention has been paid to the natural environment. The research on the prevention and control of geological disasters plays a vital role in realizing the harmonious coexistence between man and nature. Landslides are one of the most common geological disasters, accounting for 69.1% of all geological disasters in China in 2022, so it is necessary to identify and monitor such disasters effectively [1]. In recent years, Synthetic Aperture Radar Interferometry (InSAR), as a microwave remote sensing technology, has been widely used in landslide monitoring [2–5]. This technology has the advantages of a wide monitoring range, high spatial resolution, and high monitoring accuracy and has become an essential tool for landslide monitoring [6–10]. InSAR processing methods commonly include PS-InSAR, SBAS-InSAR, and IPTA technology [11]. IPTA technology is a monitoring method based on radar scattering mechanisms and polarization characteristics analysis, which has broad application prospects in landslide monitoring [12–16]. Compared with PS-InSAR and SBAS-InSAR in mountainous areas, this method selects more feature points and obtains more deformation information, which is more suitable for early landslide identification [17]. In recent years, the research on IPTA technology in landslide monitoring has made significant progress. For example, Zhang

used the method to monitor the loess landslide and found that the improved algorithm has a good performance in reducing interference points and improving monitoring accuracy and can realize monitoring at a single pixel scale [18]; Ding combined this with TerraSAR-X data to detect landslides based on methods, and found that the method based on the normalized differential polarization index has the best effect [19]; Theodoros realized the high-resolution monitoring of landslide activity by combining spaceborne SAR and ground-based GNSS data, and the results show that this method can accurately detect landslide deformation signals [20].

In sum, IPTA technology has certain advantages in landslide monitoring, but the characteristic information of InSAR results is rich. To improve the monitoring efficiency, it is necessary to remove anomalies and disturbance points adaptively. Secondly, there is a problem of the low efficiency of manual interpretation in deformation zone interpretation, and it is essential to solve the automatic interpretation mode in the present state of massive data [21,22].

To solve these problems, it is necessary to combine machine learning algorithms with InSAR technology to study the automatic interpretation method of the deformation zone. Commonly used clustering methods include k-means, mean-shift, DBSCAN, and so on. DBSCAN is a density-based clustering algorithm. Compared with other types of clustering methods, this method does not need to determine the number of clusters. It can identify noise and clusters with arbitrary shapes well, so it is widely used in the InSAR monitoring field. In 2016, Bakon combined the DBSCAN method and InSAR technology to filter out the spatial noise in the low-coherence area and highlight the details of the deformation area [23]. In 2022, Zhang classified urban center clusters by combining the DBSCAN method with the SBAS-PS InSAR and obtained the boundary between built-up and non-built areas [24]. In 2022, Talib combined PS-InSAR with DBSCAN to monitor and identify sinkholes [25]. All the above studies have achieved good results. The advantages of DBSCAN include processing large-scale data, automatically detecting anomalies and interference, and clustering InSAR data quickly and effectively.

However, DBSCAN needs to traverse all the points in clustering and calculate the distance between each two points, which is inefficient and resource intensive. Therefore, this paper proposes a model combining the HNSW and DBSCAN methods. The HNSW–DBSCAN model is more efficient than the DBSCAN nearest neighbor point search method and can complete the query of the dataset without traversing all points. We conducted experiments in the western mountainous area of Beijing to verify the efficiency and accuracy of the model.

2. Study Area and Data Preparation

2.1. Study Area

The study area is Fangshan District and Mentougou District, the southwestern gateway to Beijing, located in the western mountainous region of Beijing. The western and northern part of the study area borders Hebei Province, between 39°30′~40°10′N latitude and 115°25′~116°15′E longitude, with a total area of 3450 km^2. The study area belongs to the Taihang Mountains, with its complex lithology, and is located in the Xishan iterative fold of the Yanshan platform fold belt, which experienced tectonic solid deformation during the Indo-Chinese and Yanshan periods, forming a series of large-scale fold structures. The fracture structures are more developed. Due to the different geomorphic causes and surface morphology, there are apparent differences in terrain, slope, gully bed, soil, vegetation conditions, and the degree of geological hazards development in each geomorphic-type area. According to the morphology of landforms, the landform types in the study area are divided into middle, low, and hills.

2.2. Data Preparation

The data used the BJ-3 optical remote sensing images with 0.3 m resolution in 2022, and the data range covered the study area; a total of 80 views of RADARSAT-2 data from

September 2016 to September 2022 were included, with a satellite replay period of 24 days, a width of 150 km, a polarization mode of HH, and a spatial resolution of 5 m × 5 m. The data range is shown in Figure 1, and the image details are shown in Table 1. The accuracy of the DEM provided by USGS is 12.5 m and Table 2 shows the computer configurations used for the experiments.

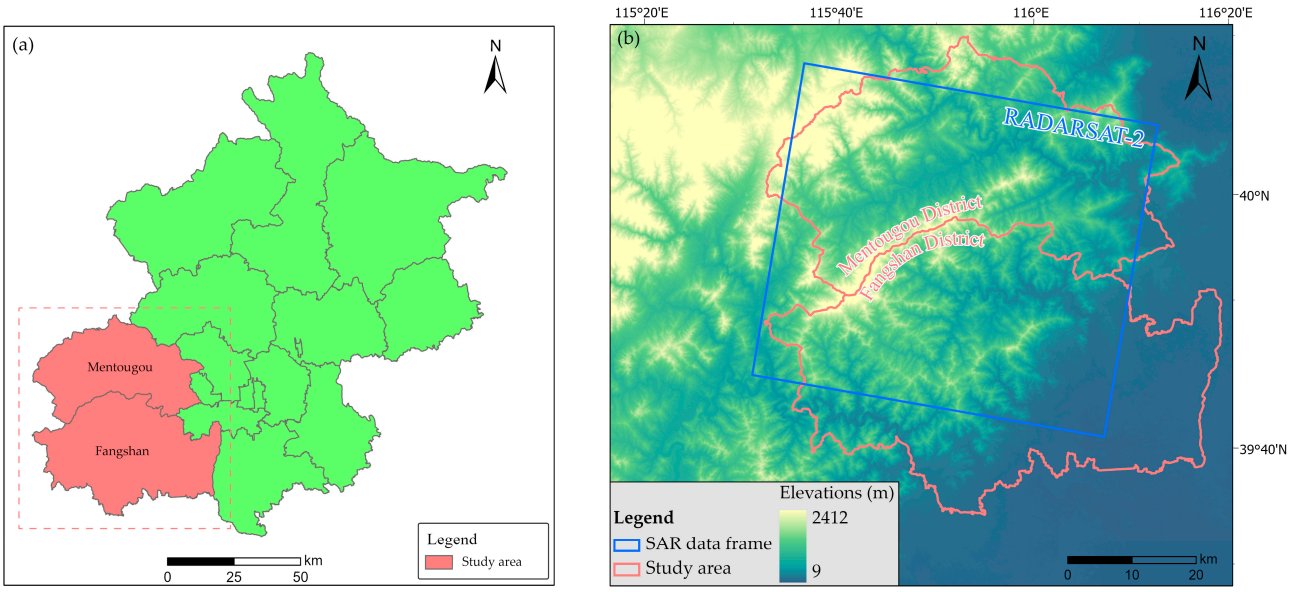

Figure 1. (**a**) Location of the study area in Beijing province. (**b**) Shade relief of DEM and the SAR data zone.

Table 1. RADARSAT-2 image details of the study area. The year is indicated vertically, and the month is displayed horizontally.

Year \ Month	1	2	3	4	5	6	7	8	9	10	11	12
2016	/	/	/	/	/	/	/	/	24	18	11	29
2017	22	15	11	4/28	22	15	/	/	19	13	6/30	24
2018	17	10	6/30	23	17	10	28	21	14	8	1/25	/
2019	12	5	1	18	12	5	23	16	9	3/27	20	14
2020	7	24	19	12	6/30	23	17	10	3/27	21	/	8
2021	1/25	18	14	7	25	18	12	5	22	16	9	3
2022	/	13	/	2/26	20	13	7/31	24	17			

Table 2. The computer configurations used for the experiments.

CPU	RAM	GPU	Solid State Drives
I9-12900KS	128 G	GTX 1660	2 T

3. Methodology

The fast identification method of hidden danger zones proposed in this paper aims to filter out the spatial noise in the InSAR results based on the spatial distribution characteristics of the deformation rate of the point targets and automatically identify the hidden danger zones in the study area. To achieve this, the IPTA-InSAR technique is utilized to obtain the annual average deformation rate. Cluster analysis is applied to divide the surface deformation regions based on the spatial distribution of deformation rates. Additionally, the range of slope units is fused, and the boundary of the hidden danger zone is determined.

The processing of the proposed method consists of five main steps:

1. N-view SAR images are acquired, and the master image is determined. The SAR dataset is then aligned with the master image as the reference.
2. The aligned SAR dataset from the previous step is processed using the IPTA technique to obtain the annual average deformation rate.
3. The surface annual average deformation rate is analyzed, and its rate standard deviation is calculated. The rate interval with a 95% confidence interval is selected based on error theory. The deformation rate within this interval is masked, and only the rates outside the interval, indicating unstable regions, are retained.
4. The coordinates of all coherent point targets and their corresponding rates are organized into a database for DBSCAN clustering analysis. The range interval of landslides in the study area is determined based on the historical hidden hazard ledger. The clustering results are filtered according to this interval, and deformation areas with smaller ranges are excluded.
5. The slope units in the study area are classified using the slope unit classification method based on the r.slopeunits method, considering the DEM data. The clustering results obtained in the previous step are fused with the slope units, and the slope units where the clustering results are located are retained. Finally, fusing the slope parameters determines the final InSAR-identified hidden slope bodies.

Please refer to the flowchart below for a visual representation of the proposed method, as shown in Figure 2:

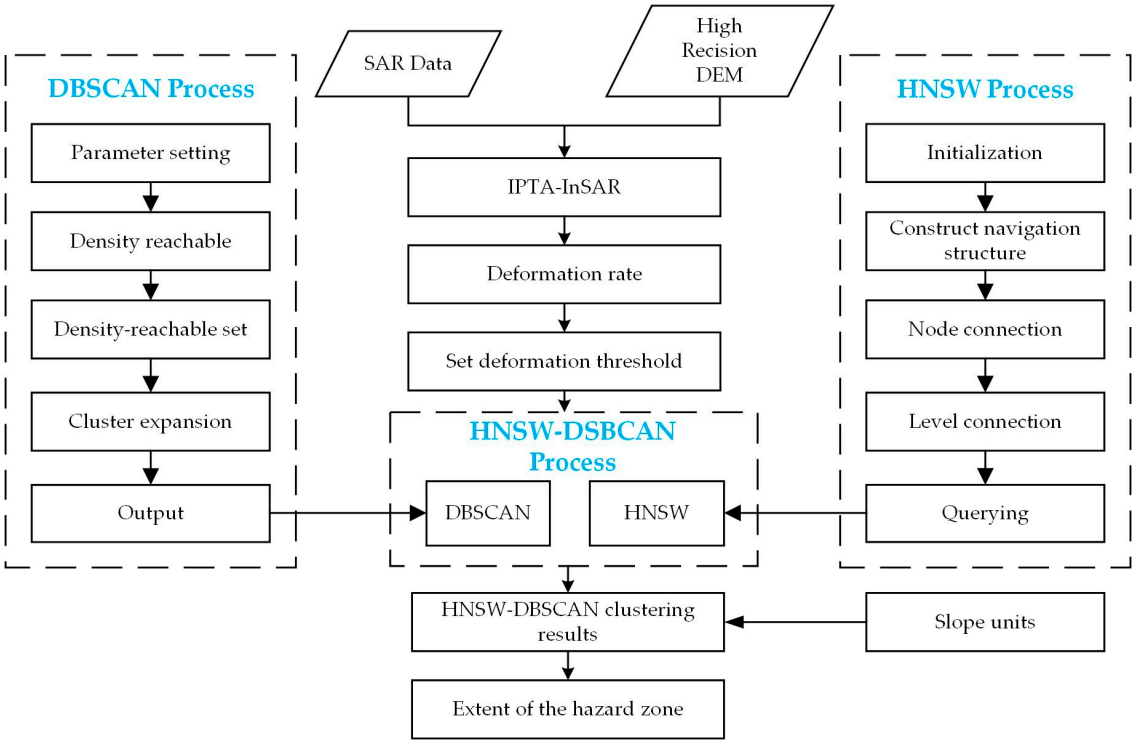

Figure 2. The Flowchart of the HNSW–DBSCAN automatic delineation method for InSAR deformation zones.

3.1. Interferometry Point Target Analysis Method

In this paper, the ground surface deformation rate is solved using the IPTA technique for the SAR data set, and its flow chart is shown in Figure 3.

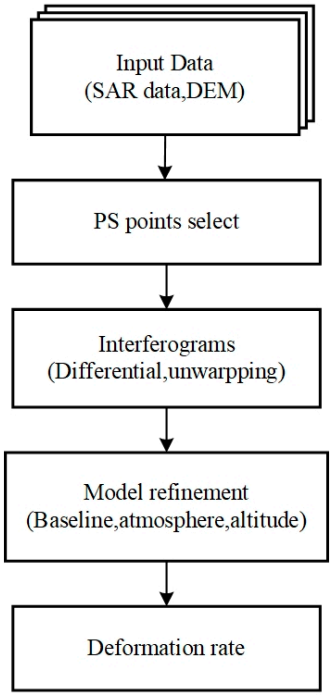

Figure 3. The flowchart of IPTA monitoring.

3.1.1. Persistent Scatterer Selection

Due to the high vegetation coverage in the study area, the traditional PS point selection method is used to achieve better results. This paper uses three-point selection strategies to select PS points to obtain target points with high phase quality and comprehensive coverage, namely, amplitude departure index method, spectral coherence, and phase stability [26,27].

3.1.2. Differential Interferometry

For a point p_i on the SAR image, the slave image interferes with the master image separately to obtain the differential interferometric phase, which consists of different components, and the interferometric phase model of IPTA is the same as the conventional InSAR model, as follows:

$$\varphi_{unw}(p_i) = \varphi_{topo}(p_i) + \varphi_{def}(p_i) + \varphi_{atm}(p_i) + \varphi_{noise}(p_i) \quad (1)$$

where $\varphi_{unw}(p_i)$ denotes the phase after untwisting, $\varphi_{topo}(p_i)$ denotes the topographic phase, $\varphi_{def}(p_i)$ denotes the deformation phase, $\varphi_{atm}(p_i)$ denotes the atmospheric phase, and $\varphi_{noise}(p_i)$ is the noise phase. Except for the noise phase, the rest of the phases can be removed by the model, and the noise phase can be removed by the filtering method where the relationship between φ_{def} and the LOS vector shape variable Δd is as follows:

$$\varphi_{def} = \frac{4\pi}{\lambda}\Delta d \quad (2)$$

where λ denotes the wavelength.

3.1.3. Model Refinement

The atmospheric delay and nonlinear deformation phases are spatially correlated at a particular spatial scale. The atmospheric delay phase and nonlinear deformation phase can be weakened by constructing a Delaunay triangular network for the point target and then making a quadratic difference between the differential interferometry phase of the

neighboring point target. The quadratic differential phase model based on the neighboring point targets is as follows:

$$\Delta\varphi = \frac{-4\pi B_{\perp}}{\lambda R sin\theta}\Delta dh - \frac{4\pi}{\lambda}\Delta v * t + \Delta\varphi_{res} \quad (3)$$

where Δdh denotes the elevation correction of the target at adjacent points, Δv denotes the deformation rate difference, and $\Delta\varphi_{res}$ denotes the residual phase, including nonlinear deformation phase, atmospheric phase, and noise phase. The model's parameters are corrected by iterative correction, and the deformation rate is finally obtained by leveling the triangular network.

3.2. DBSCAN

DBSCAN clustering algorithm is a density-based clustering algorithm that can divide data points into core points and noise according to the density of points in the neighborhood. Clusters of different shapes can be identified by continuously delineating the points within the clusters. The spatial noise in the data set can also be removed by changing the parameter threshold. Unlike the currently popular K-means algorithm, this method does not need to realize the setting of the number of clusters, and it can effectively identify clusters of any shape. It can identify noisy points, which is widely used.

The DBSCAN algorithm has two essential parameters: the neighborhood radius Eps and the density threshold MinPts for point A(i, j) and point B(m, n), where A, B$\in$ D. Neighborhood radius eps means that, with A as the center of the circle, the radius is within the area of eps as a circle; density threshold MinPts implies that, for point A, if there exist at least MinPts points within the neighborhood radius, then A can be designated as the core point. The specific flow of the DBSCAN algorithm is as follows:

(1) Select point A in dataset D, count all the points in the neighborhood eps of point A, and write the neighborhood as $Num_{eps}(A)$, if $Num_{eps}(A) \geq$ MinPts, mark point as the core point and establish the cluster core point at the same time; if $Num_{eps}(A) <$ MinPts, the point is a noise point.
(2) Select the next point within $Num_{eps}(A)$ in the neighborhood B(m, n), and add $Num_{eps}(B)$ to $Num_{eps}(A)$ in the same step as the previous one.
(3) Repeat step 2 until all the points in the $Num_{eps}(A)$.
(4) Repeat steps 1–3 until all points in dataset D are traversed and marked as core points or noise.

3.3. Hierarchical Navigable Small Worlds and DBSCAN

HNSW is an efficient nearest neighbor search algorithm that constructs a multi-level graph structure where the nodes at each level represent a vector and a certain number of candidate nodes are reserved in each level of the graph, and the candidate nodes are also connected to their candidate nodes. As shown in Figure 4, to find the nearest neighbors of a vector, candidate nodes are filtered by traversing down from the higher levels until the nearest node to the query vector is found. By adjusting the number of candidate nodes to balance the speed and accuracy of the search, HNSW can perform an efficient nearest-neighbor search in high-dimensional data. This paper uses the open-source code of HNSW [28].

As shown in Figure 5, the process of finding the nearest neighbor points of a given input point (represented by the red dot) begins with the initial step of querying N candidate points around the input point. The closest point to the input point is then found based on the Euclidean distance and is denoted as Q_2. At the same time, the candidate points are marked to avoid repeated queries and improve retrieval efficiency. Next, the candidate points are queried similarly to find their own set of candidate points and determine their nearest neighbor to the input point, denoted as Q_1. This process repeats until the closest point to the query point in all layers (denoted as Q_0) is found, completing the search for the nearest neighbor points of the input point. By utilizing the HNSW (Hierarchical Navigable Small

World) algorithm, space consumption and query time can be effectively reduced when applied to DBSCAN spatial search technique, resulting in improved clustering efficiency. The technical steps are summarized below.

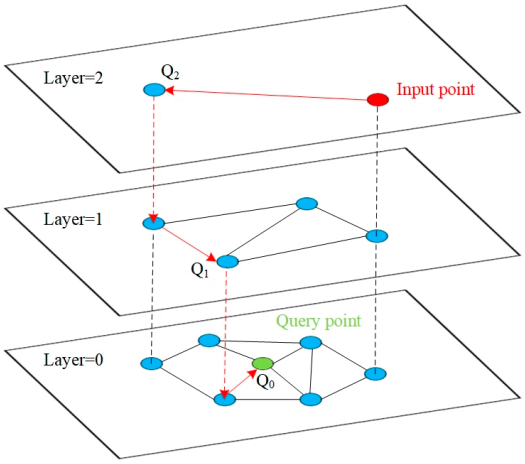

Figure 4. HNSW algorithm diagram.

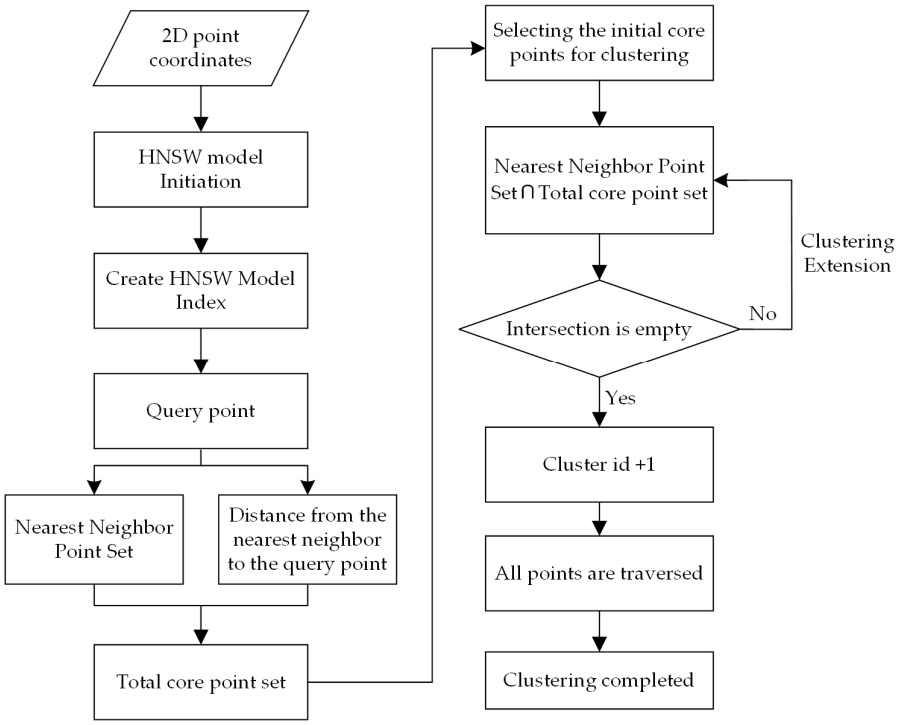

Figure 5. The flowchart of the HNSW-DBSCAN method.

4. Results and Analysis

4.1. Result of IPTA Processing

The IPTA (Interferometric Point Target Analysis) technique has shown good processing results for areas with long time spans and high vegetation coverage. This study employed the IPTA technique by GAMMA SOFTWARE 2020 to select point targets based on their spectral properties and scattering stability. Specifically, we applied the IPTA technique to process 80 scenes of RADARSAT-2 data and selected 72,026,685 point targets. The interferometric combination of multiple master images was used, as shown in Figure 6. Precise orbit data were also used for preprocessing to minimize orbit errors.

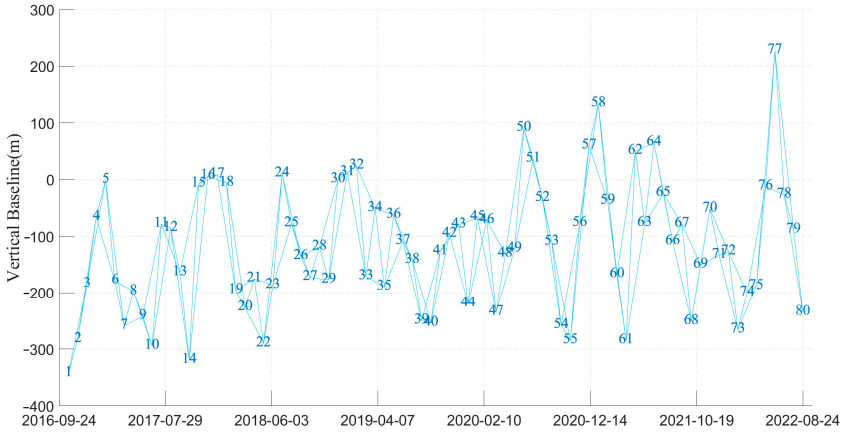

Figure 6. The spatiotemporal baselines of IPTA.

After IPTA processing, the surface deformation rate and temporal deformation results from 2016 to 2022 were obtained, and the results were displayed by geocoding, as shown in Figures 7 and 8.

According to Figure 7, the study area is generally stable, and the main deformation zones are concentrated in the Shijiaying Township, Da'anshan Township, and Datai Township, as shown in the red mark in Figure 7. According to the geological data, the surrounding rock types are mainly shale, siltstone, and soft rock coal seams. InSAR identified twenty deformation zones in this study area, and ten of them were confirmed as landslide hazards after on-site investigation. The deformation rate of landslide is 30.5 mm/year at the maximum and 5.8 mm/a at the minimum; the area of the landslide body is uneven in size, with a maximum area of 820,000 m^2 and a minimum area of 1600 m^2.

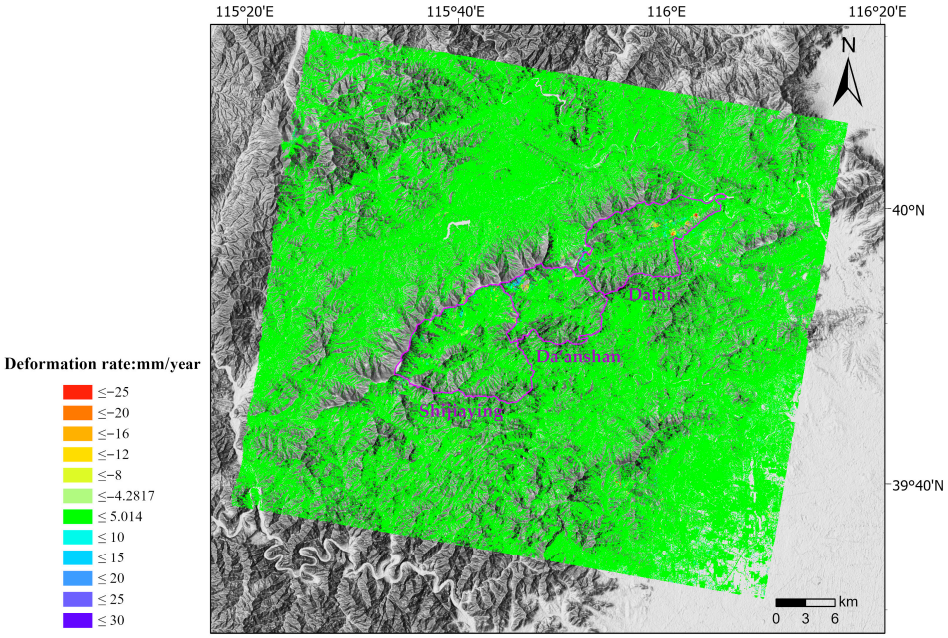

Figure 7. The deformation velocity of the study area was obtained by IPTA.

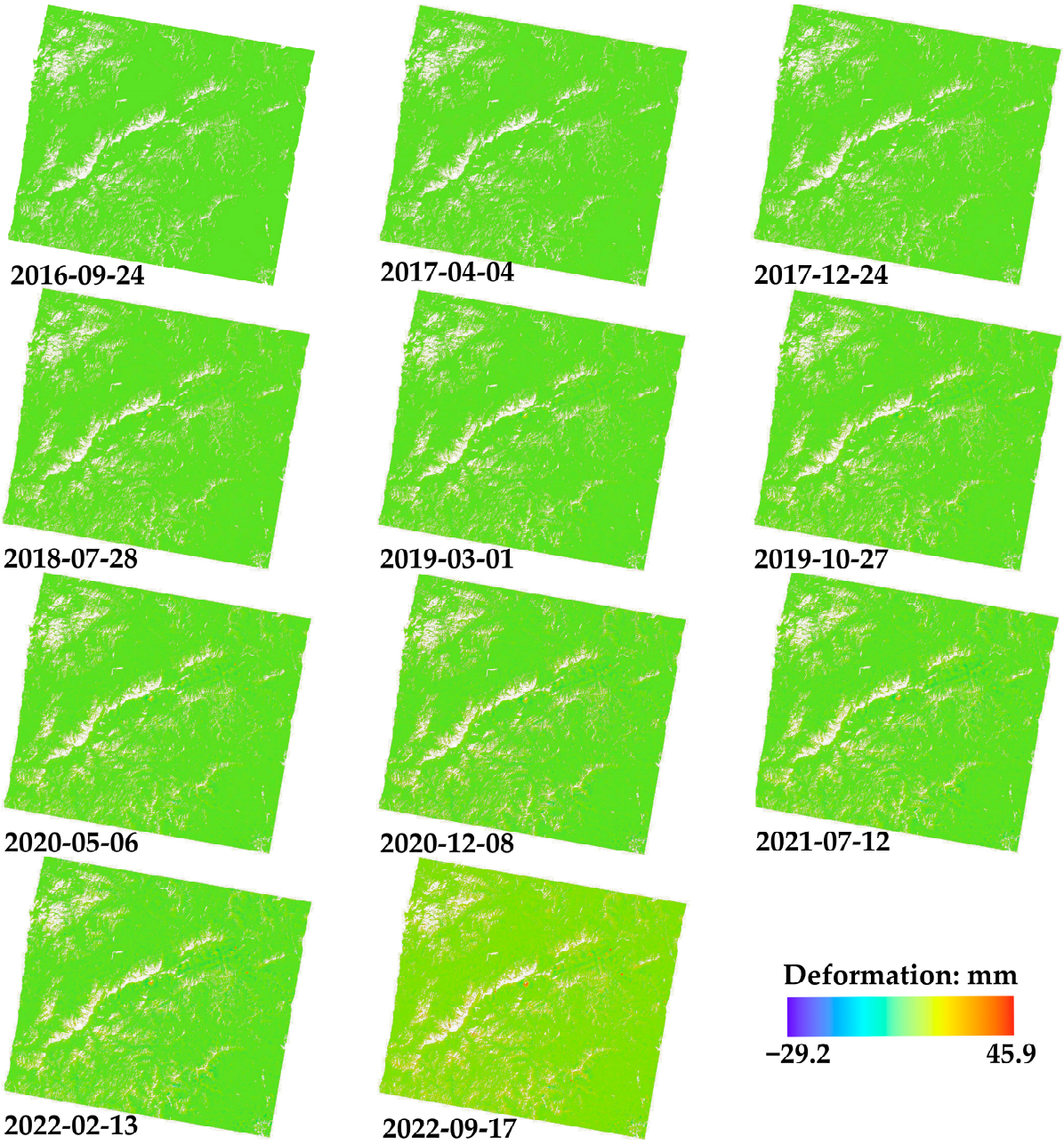

Figure 8. Time series diagram of surface deformation.

4.2. HNSW–DBSCAN

First of all, the InSAR deformation rate needs to be divided into stable and unstable regions according to the threshold, so a deformation stability threshold needs to be determined, and, theoretically, the deformation of stable points should be 0, but the accuracy of InSAR deformation monitoring results vary with different regions due to the accuracy of the data processing methods, and there are no uniform threshold delineation results. The experimental analysis shows that the approximate accuracy information of the InSAR results can be used to determine the deformation rate range of the stable region. In this paper, the 95% confidence interval (1.96 times STD) is used to delineate the boundary between the stable area and the deformation region, and the deformation rate range of the stable region is finally obtained as $[-4.2817\ \mathrm{mm/a}, 5.014\ \mathrm{mm/a}]$, as shown in Figure 9.

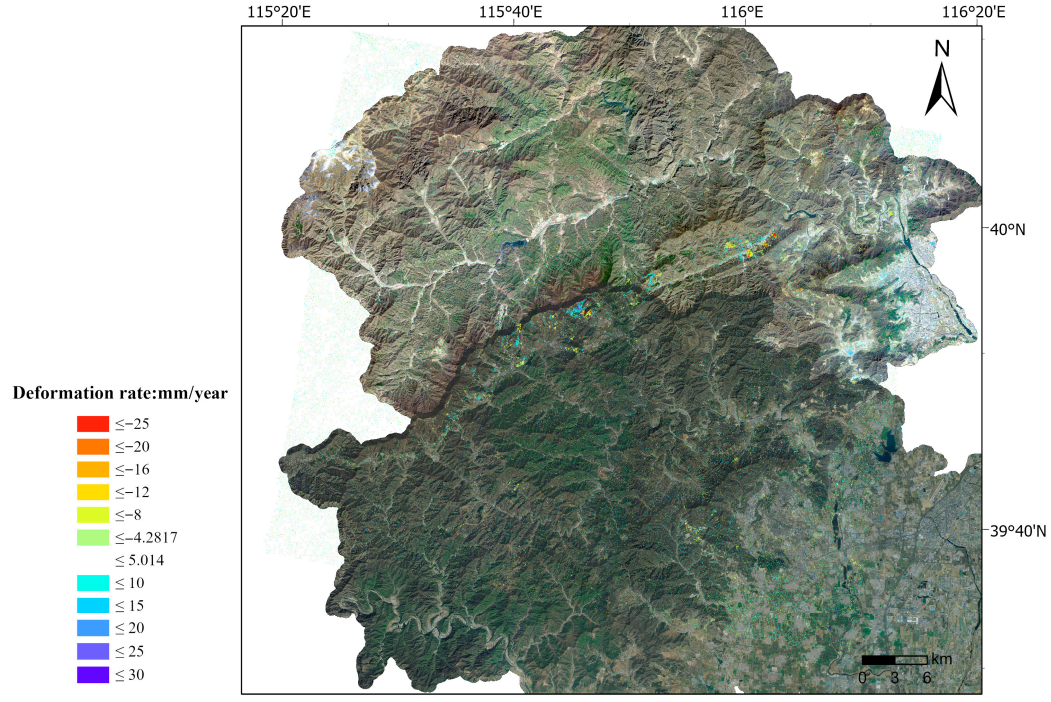

Figure 9. Deformation rate after threshold division.

The number of non-stable areas visible in Figure 9 is large, and the delineation of deformation zones at this time will identify many of them, which is a great difficulty for field investigation, and this paper uses the HNSW–DBSCAN algorithm to screen the deformation zones. The results are shown in Figure 10.

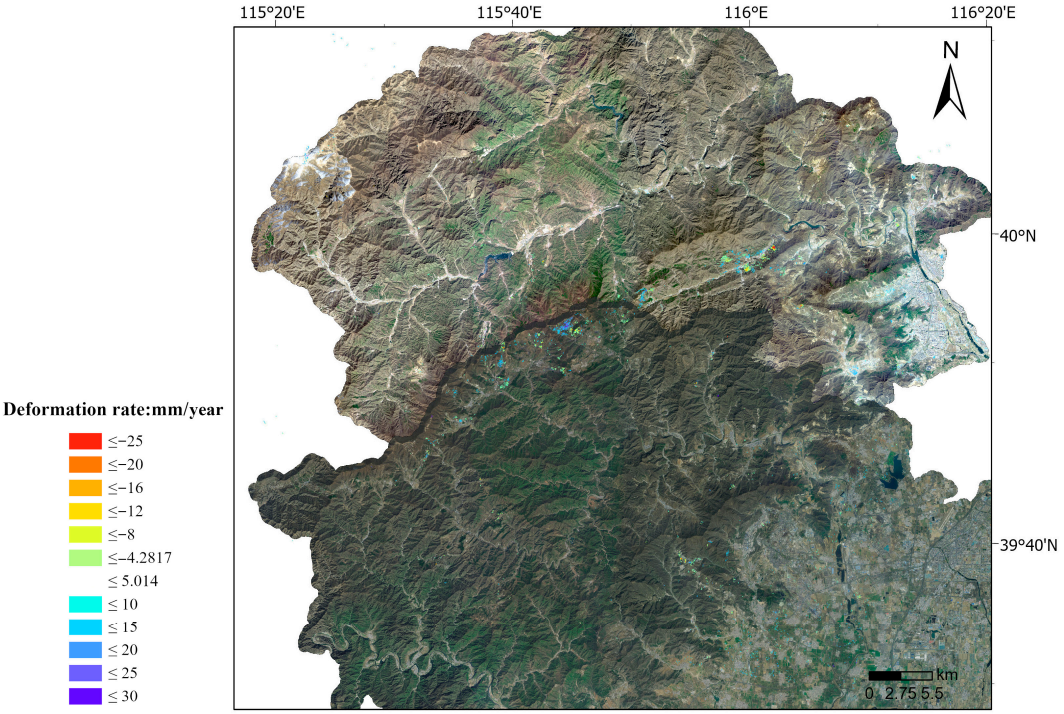

Figure 10. The result of the HNSW–DBSCAN.

After HNSW–DBSCAN clustering, the noise in the study area is removed, but there is still a small area of deformation aggregation affecting the interpretation. To interpret the deformation of the prominent area more reasonably, this paper selects the landslide area threshold and keeps the clusters in which the number of pixels exceeds the threshold.

After testing, for the Xishan test area, the landslide hazard area in the ground hazard ledger is converted into the number of pixel points according to the resolution of SAR data of 5 × 5 m. The total number of pixel statistics is plotted in Table 3, and the smallest identifiable landslide is selected to set the landslide area threshold.

Table 3. Total number of pixels statistics table.

Total Pixels	<100	<400	<1000	<2000	≥2000	Total
Number	10	14	12	9	8	53

Therefore, for the InSAR interpretation of the deformation area, the scanning radius of the DBSCAN algorithm is set to five pixels, which corresponds to a horizontal distance of 25 m, and the minimum number of included pixels is twenty pixels, and a total of 23,416 different deformation clusters are obtained. By counting the distribution of the number of pixels occupied by different landslides, the landslide decoding threshold was selected according to the characteristics of geological hazards in Beijing, and the deformation potential areas were determined. The process of deformation area circling around Shijiaying and Da'anshan is shown in Figure 11a–c. Finally, 713 deformation zones were identified in the study area, as shown in Figure 11.

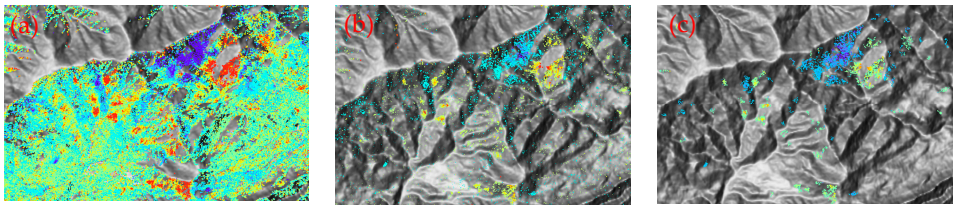

Figure 11. The result of HNSW–DBSCAN. (**a**). Raw InSAR rate map. (**b**). After deformation threshold screening. (**c**). After clustering analysis.

After clustering using HNSW–DBSCAN, 11,641 different deformation clusters were obtained. Based on the characteristics of regional geological hazards in the study area, the minimum identifiable landslide area was selected as the threshold value to determine the potential deformation area. Figure 11a–c shows the process of deformation zone enclosure around Jinjitai village in the Shijiaying area of Fangshan District. Because the occurrence of landslides is related to the slope of the mountain, this paper uses the slope threshold of landslides to retain the areas where landslides are more likely to occur. Finally, 713 deformation zones were identified in the study area. The finalized map of the extent of deformed slopes was obtained by fusing with the slope units generated by the r.slopeunits software for GRASS 7.8 [29], as shown in Figure 12.

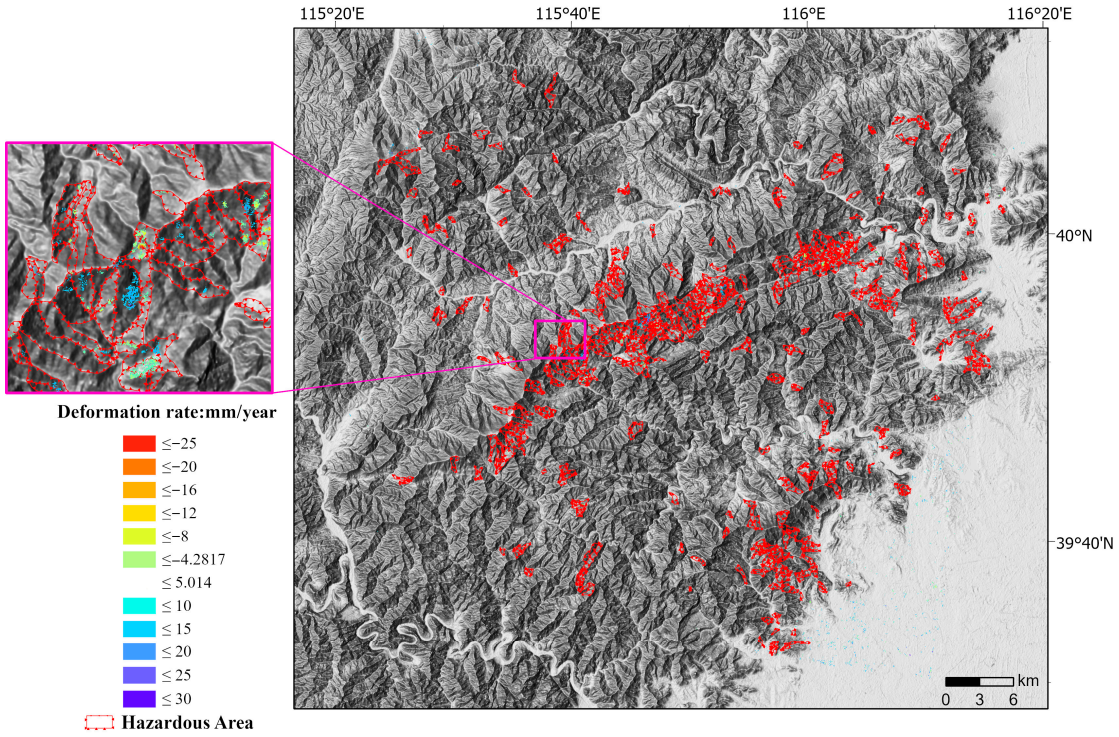

Figure 12. Range of automatically identified deformation zones.

4.3. Comparison between Traditional DBSCAN and HNSW–DBSCAN

The current clustering methods for point density mainly include the DBSCAN and KD-TREE DBSCAN methods. The HNSW–DBSCAN method proposed in this paper has higher efficiency for the above two ways on the nearest neighbor problem. To verify the method's effectiveness, the three methods are used in this paper for comparison experiments on the 2D manual dataset. By comparing the accuracy and clustering efficiency of the three methods on different test sets, the feasibility of the HNSW–DSBCAN method is demonstrated.

To better verify their clustering accuracy, the three methods were tested using test datasets, and Figure 13 shows the four manual test datasets: d6, ls3, t4, and t7. The time and correct rate of the three methods on different data sets are counted separately, and the time comparison is plotted in Figure 14. The clustering performance evaluation indicators are shown in Table 4. According to Figure 14 and Table 4, it can be seen that the proposed method outperforms the other two methods in terms of time and correct rate, which shows that the proposed method can guarantee the correct clustering rate and improve efficiency at the same time and has a better performance in InSAR decoding has higher practicality.

Table 4. Clustering algorithm evaluation metrics.

Data	Adjust Rand Index	Homogeneity	Completeness	V-Measure
d6	98.7%	96.3%	96.4%	96.4%
l3	98.7%	97.7%	97.5%	97.6%
t4	98.6%	97.3%	97.4%	97.4%
t7	96.4%	94.7%	92.1%	93.4%

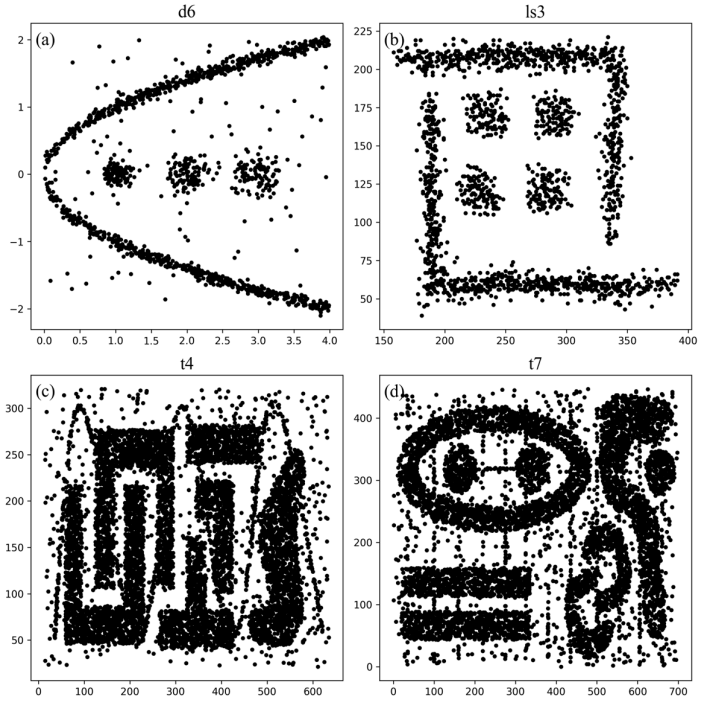

Figure 13. Test data set, where (**a**) is the d6 dataset with 1400 instances, (**b**) is the ls3 dataset with 1735 instances, (**c**) is the t4 dataset with 8000 instances, and (**d**) is the t7 dataset with 8000 instances.

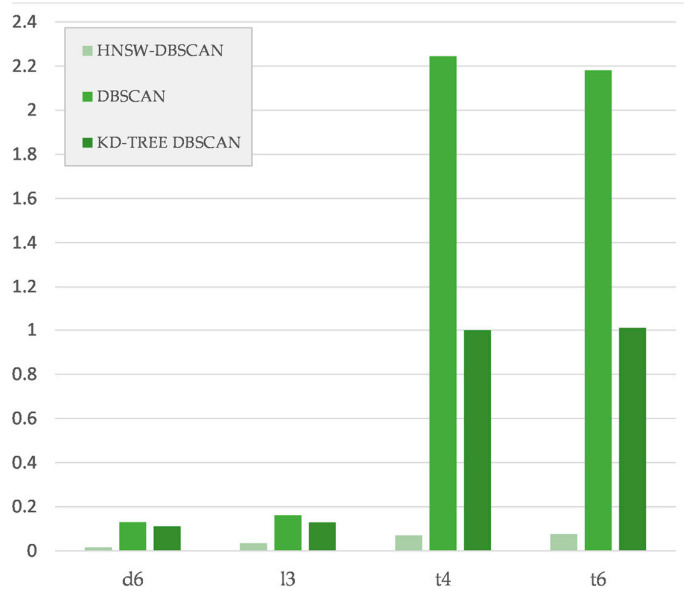

Figure 14. Histogram of time statistics used for the four data sets.

The above analysis is based on the accuracy evaluation of the classification results of each point in the clustering results. For the interpretation of the InSAR deformation zone, small clustering errors in the clustering results will not affect the interpretation results, because when there are a certain number of deformation points in the slope unit, they will be identified as landslides. For automatic identification, the main evaluation index is the accuracy of landslide interpretation, so the accuracy of the automatic identification of landslides is tested based on the landslide determined by InSAR results. It is verified that the landslides found in the field investigation in the study area are all in the automatic interpretation results, which proves the effectiveness of this method in the InSAR interpretation of landslides.

5. Discussion

For the landslide body after IPTA interpretation, the landslide on the west side of Ash Qingjian village in Shijiaying Township, Fangshan District, was used as a typical landslide to analyze its deformation pattern and signs of deformation [30]. The landslide is located in the middle reaches of the Anzhi ditch of Ash Qingjian, and there are two collapses on the front edge of this hidden body on the optical image, and one tension crack is produced on the rear edge. The historical images from 2003 to 2019 show that the lower slope of this landslide's hidden body collapses first and then drives the upper slope to slide, which makes the tension crack appear on the rear edge of the landslide body, showing the characteristic of a traction landslide (Figure 15); Figure 16 represents the deformation rate of the landslide, point P-1 is located in the upper part of the landslide body, point P-2 is located in the middle of the landslide body, and point P-3 is located in the lower part of the landslide body. Figure 17 represents the time-series deformation rates of the three studied points. The rate of deformation of the upper part of the landslide body is lower than that of the middle and lower parts of the landslide body, and the upper part of the landslide body has developed several tension fissures and formed a multi-stage dislocation of different heights. At this stage, the deformation and damage of the landslide body is mainly in the form of pulling and cracking at the back edge and bulging at the front edge.

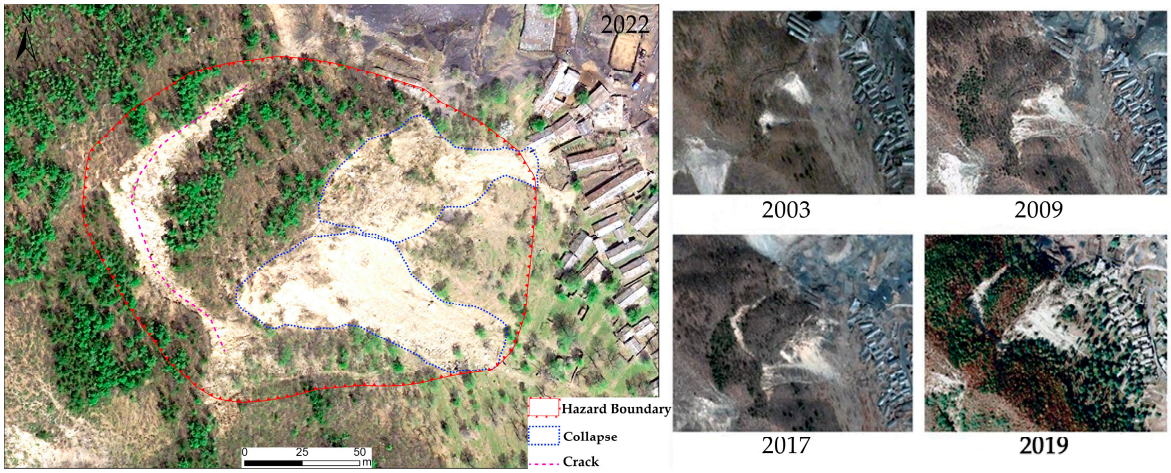

Figure 15. Optical remote sensing interpretation features (2003, 2009, 2017, 2019, and 2022).

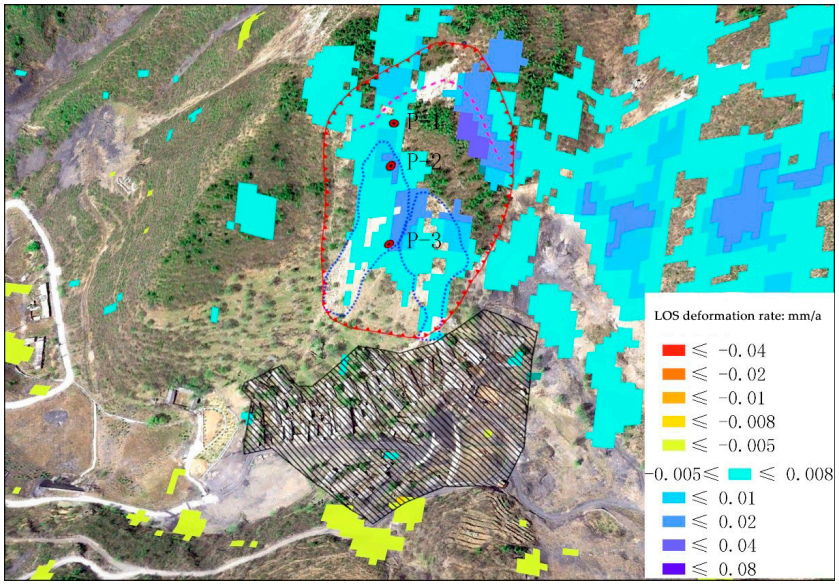

Figure 16. Landslide deformation rate.

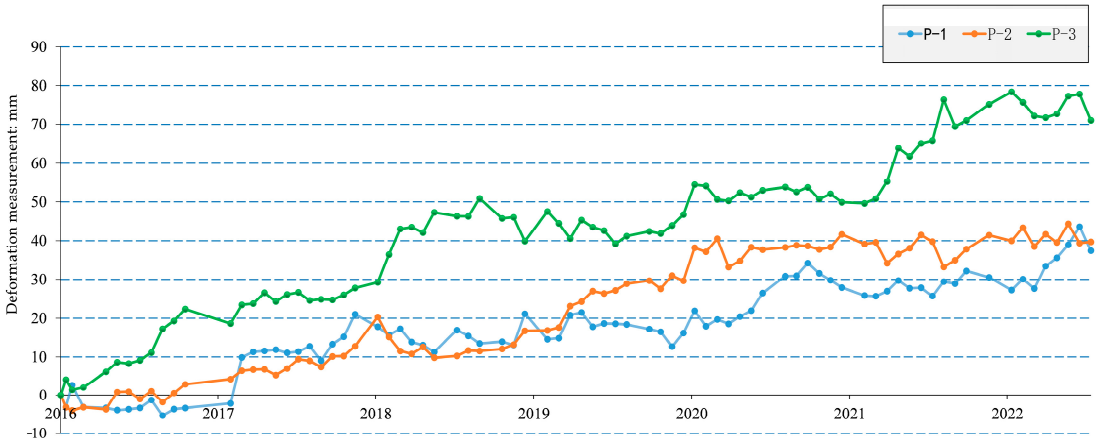

Figure 17. Deformation time series curve.

Through field verification, the accuracy of the proposed method for landslide identification is proved, and it is proved that IPTA technology can not only delineate the boundary and spatial distribution of landslides but also directly reflect the creep and disaster process of landslides in the time domain, which can play an important role in landslide monitoring and warning. Moreover, international scholars have found that IPTA technology can realize high-precision deformation monitoring in different climate regions, so the automatic deformation interpretation method proposed in this paper is still applicable in different climate regions. Due to the limitation of the nderlying code, the proposed method has not fully developed its performance and still has room for efficiency improvement.

6. Conclusions

InSAR technology has been widely used in landslide deformation zone identification, but there are still problems with interpretation relying on expert experience, subjectivity, and low interpretation efficiency. To solve this problem, a full process method of automatic deformation zone interpretation is proposed, which reduces the process of manual participation, releases productivity, and increases productivity from temporal InSAR processing to automatic deformation zone interpretation and the circling of deformation zones.

1. This paper proposes the HNSW–DBSCAN algorithm, which combines the HNSW and DBSCAN methods. The algorithm is tested using Beijing Xishan Mountain as the study area. The results show that the algorithm effectively removes spatial noise and greatly improves clustering efficiency while maintaining high accuracy compared with traditional methods.
2. This paper introduces a method that combines slope units with clustering results to identify the slopes where deformation occurs efficiently. This approach aims to enhance InSAR decoding efficiency and enable the rapid targeting of deformation areas.
3. IPTA technology was employed to monitor surface deformation in the Xishan area of Beijing. The accuracy of the results from IPTA technology in highly vegetation-covered mountainous areas was verified through in-conformity accuracy verification. Furthermore, field validation was conducted to confirm the decoded landslides, and the validation results were found to be consistent with the InSAR decoding results.

It has been verified that the automatic interpretation method proposed in this paper has been improved in efficiency and has high accuracy. This method provides an effective automatic interpretation method for the subsequent InSAR interpretation which is significant for early deformation recognition. In the following research, we will study the adaptive automatic recognition work and select different regions for method validation.

Author Contributions: J.H.: writing—original draft preparation; X.G., R.J., Y.N., H.Y., D.Z., X.N., S.W., C.Y., C.M., X.M. and J.Z.: data curation. All authors have read and agreed to the published version of the manuscript.

Funding: This work was funded by the Project of Beijing sudden geological disaster monitoring and early warning system (11000023T000002124048); the early identification and early warning of typical geological disasters in Xishan, Beijing Demonstration Study (11000022T000001362678); and the intelligent early identification method and prevention countermeasures of typical geological hazards in Beijing (bjkx202311).

Data Availability Statement: DEM data used in this study were provided by USGS at https://search.asf.alaska.edu/#/, accessed on 1 June 2021.

Acknowledgments: We are very grateful for the 12.5 m resolution DEM from the National Aeronautics and Space Administration (NASA), TAY for providing the r.slopeunits software for GRASS 7.8.

Conflicts of Interest: The authors declare no conflict of interest.

References

1. Ministry of Natural Resources of the People's Republic of China. Statistical Bulletin of China's Natural Resources in 2022. Available online: https://www.mnr.gov.cn/sj/tjgb.html (accessed on 1 April 2023).
2. Zhao, J.; Chen, Q.; Yang, Y.; Xu, Q. Coseismic Faulting Model and Post-Seismic Surface Motion of the 2023 Turkey–Syria Earthquake Doublet Revealed by InSAR and GPS Measurements. *Remote Sens.* **2023**, *15*, 3327. [CrossRef]
3. Liu, Y.; Cao, W.; Shi, Z.; Yue, Q.; Chen, T.; Tian, L.; Zhong, R.; Liu, Y. Evaluation of Post-Tunneling Aging Buildings Using the InSAR Nonuniform Settlement Index. *Remote Sens.* **2023**, *15*, 3467. [CrossRef]
4. Li, Z.; Dai, K.; Deng, J.; Liu, C.; Shi, X.; Tang, G.; Yin, T. Identifying Potential Landslides in Steep Mountainous Areas Based on Improved Seasonal Interferometry Stacking-InSAR. *Remote Sens.* **2023**, *15*, 3278. [CrossRef]
5. Gao, H.; Xiong, L.; Chen, J.; Lin, H.; Feng, G. Surface Subsidence of Nanchang, China 2015–2021 Retrieved via Multi-Temporal InSAR Based on Long- and Short-Time Baseline Net. *Remote Sens.* **2023**, *15*, 3253. [CrossRef]
6. Kumar Maurya, V.; Dwivedi, R.; Ranjan Martha, T. Site scale landslide deformation and strain analysis using MT-InSAR and GNSS approach—A case study. *Adv. Space Res.* **2022**, *70*, 3932–3947. [CrossRef]
7. Liu, X.; Zhao, C.; Zhang, Q.; Lu, Z.; Li, Z.; Yang, C.; Zhu, W.; Liu-Zeng, J.; Chen, L.; Liu, C. Integration of Sentinel-1 and ALOS/PALSAR-2 SAR datasets for mapping active landslides along the Jinsha River corridor, China. *Eng. Geol.* **2021**, *284*, 106033. [CrossRef]
8. Dong, J.; Liao, M.; Xu, Q.; Zhang, L.; Tang, M.; Gong, J. Detection and displacement characterization of landslides using multi-temporal satellite SAR interferometry: A case study of Danba County in the Dadu River Basin. *Eng. Geol.* **2018**, *240*, 95–109. [CrossRef]
9. Kiseleva, E.; Mikhailov, V.; Smolyaninova, E.; Dmitriev, P.; Golubev, V.; Timoshkina, E.; Hooper, A.; Samiei-Esfahany, S.; Hanssen, R. PS-InSAR Monitoring of Landslide Activity in the Black Sea Coast of the Caucasus. *Procedia Technol.* **2014**, *16*, 404–413. [CrossRef]
10. Dong, J.; Zhang, L.; Liao, M.; Gong, J. Improved correction of seasonal tropospheric delay in InSAR observations for landslide deformation monitoring. *Remote Sens. Environ.* **2019**, *233*, 111370. [CrossRef]
11. Novellino, A.; Cesarano, M.; Cappelletti, P.; Di Martire, D.; Di Napoli, M.; Ramondini, M.; Sowter, A.; Calcaterra, D. Slow-moving landslide risk assessment combining Machine Learning and InSAR techniques. *Catena* **2021**, *203*, 105317. [CrossRef]
12. Zhou, Z.; Yao, X.; Ren, K.; Liu, H. Formation mechanism of ground fissure at Beijing Capital International Airport revealed by high-resolution InSAR and numerical modelling. *Eng. Geol.* **2022**, *306*, 106775. [CrossRef]
13. Cai, J.; Liu, G.; Jia, H.; Zhang, B.; Wu, R.; Fu, Y.; Xiang, W.; Mao, W.; Wang, X.; Zhang, R. A new algorithm for landslide dynamic monitoring with high temporal resolution by Kalman filter integration of multiplatform time-series InSAR processing. *Int. J. Appl. Earth Obs.* **2022**, *110*, 102812. [CrossRef]
14. Lu, P.; Bai, S.; Tofani, V.; Casagli, N. Landslides detection through optimized hot spot analysis on persistent scatterers and distributed scatterers. *Isprs J. Photogramm.* **2019**, *156*, 147–159.
15. Ma, P.; Li, T.; Fang, C.; Lin, H. A tentative test for measuring the sub-millimeter settlement and uplift of a high-speed railway bridge using COSMO-SkyMed images. *Isprs J. Photogramm.* **2019**, *155*, 1–12. [CrossRef]
16. Chen, F.; Lin, H.; Zhou, W.; Hong, T.; Wang, G. Surface deformation detected by ALOS PALSAR small baseline SAR interferometry over permafrost environment of Beiluhe section, Tibet Plateau, China. *Remote Sens. Environ.* **2013**, *138*, 10–18. [CrossRef]
17. Wang, Y.; Feng, G.; Li, Z.; Xu, W.; Wang, H.; Hu, J.; Liu, S.; He, L. Estimating the long-term deformation and permanent loss of aquifer in the southern Junggar Basin, China, using InSAR. *J. Hydrol.* **2022**, *614*, 128604. [CrossRef]
18. Haibo, Z.; Zongchun, L.; Bing, X. Ground Subsidence Monitoring Using Interferometric Point Target Analysis. *J. Geomat. Sci. Technol.* **2016**, *33*, 145–149.
19. Rongrong, D.; Jia, X.U.; Xiaobin, L.; Kang, X.U. Monitoring of surface subsidence using PSInSAR with TerraSAR-X high-resolution data. *Remote Sens. Land Resour.* **2015**, *27*, 158–164.

20. Gatsios, T.; Cigna, F.; Tapete, D.; Sakkas, V.; Pavlou, K.; Parcharidis, I. Copernicus Sentinel-1 MT-InSAR, GNSS and Seismic Monitoring of Deformation Patterns and Trends at the Methana Volcano, Greece. *Appl. Sci.* **2020**, *10*, 6445. [CrossRef]
21. Chen, Z.; Zhang, L.; Zhang, G. An improved InSAR image co-registration method for pairs with relatively big distortions or large incoherent areas. *Sensors* **2016**, *16*, 1519. [CrossRef]
22. Wang, S.; Zhang, G.; Chen, Z.; Xu, Z.; Liu, Y. A refined parallel stacking InSAR workflow for large-scale deformation fast extraction—A case study of Tibet. *Geocarto Int.* **2022**, *37*, 16074–16085. [CrossRef]
23. Bakon, M.; Oliveira, I.; Perissin, D.; Sousa, J.; Papco, J. A data mining approach for multivariate outlier detection in heterogeneous 2D point clouds: An application to post-processing of multi-temporal InSAR results. In Proceedings of the 2016 IEEE International Geoscience and Remote Sensing Symposium (IGARSS), Beijing, China, 10–15 July 2016; pp. 56–59.
24. Zhang, P.; Guo, Z.; Guo, S.; Xia, J. Land Subsidence Monitoring Method in Regions of Variable Radar Reflection Characteristics by Integrating PS-InSAR and SBAS-InSAR Techniques. *Remote Sens.* **2022**, *14*, 3265. [CrossRef]
25. Talib, O.; Shimon, W.; Sarah, K.; Tonian, R. Detection of sinkhole activity in West-Central Florida using InSAR time series observations. *Remote Sens. Environ.* **2022**, *269*, 112793. [CrossRef]
26. Han, J.; Yang, H.; Liu, Y.; Lu, Z.; Zeng, K.; Jiao, R. A Deep Learning Application for Deformation Prediction from Ground-Based InSAR. *Remote Sens.* **2022**, *14*, 5067. [CrossRef]
27. Liu, Y.; Yang, H.; Fan, J.; Han, J.; Lu, Z. NL-MMSE: A Hybrid Phase Optimization Method in Multimaster Interferogram Stack for DS-InSAR Applications. *IEEE J.-Stars.* **2022**, *15*, 8332–8345. [CrossRef]
28. Malkov, Y.A.; Yashunin, D.A. Efficient and Robust Approximate Nearest Neighbor Search Using Hierarchical Navigable Small World Graphs. *IEEE Trans. Pattern Anal. Mach. Intell.* **2020**, *42*, 824–836. [CrossRef]
29. Alvioli, M.; Marchesini, I.; Reichenbach, P.; Rossi, M.; Ardizzone, F.; Fiorucci, F.; Guzzetti, F. Automatic delineation of geomorphological slope units with r.slopeunits v1.0 and their optimization for landslide susceptibility modeling. *Geosci. Model Dev.* **2017**, *9*, 3975–3991. [CrossRef]
30. Jiao, R.; Wang, S.; Yang, H.; Guo, X.; Han, J.; Pei, X.; Yan, C. Comprehensive Remote Sensing Technology for Monitoring Landslide Hazards and Disaster Chain in the Xishan Mining Area of Beijing. *Remote Sens.* **2022**, *14*, 4695. [CrossRef]